Surface & Coatings Technology 236 (2013) 476–484

Contents lists available at ScienceDirect

Surface & Coatings Technology

journal homepage: www.elsevier.com/locate/surfcoat

Silica-based hybrid coatings for corrosion protection of carbon steel. Part I: Effect of pretreatment with phosphoric acid

Ianina Santana [a], Andrés Pepe [a], Emilio Jimenez-Pique [b], Sergio Pellice [a], Silvia Ceré [a,*]

[a] INTEMA, Universidad Nacional de Mar del Plata — CONICET, Juan B. Justo 4302, B7608FDQ, Mar del Plata, Argentina
[b] Departament de Ciència dels Materials i Enginyeria Metallúrgica, Universitat Politècnica de Catalunya, Avda. Diagonal, 647 (ETSEIB), 08028 Barcelona, Spain

ARTICLE INFO

Article history:
Received 22 April 2012
Accepted in revised form 29 July 2012
Available online 13 September 2012

Keywords:
AISI 1010
Phosphoric acid treatment
EIS
Corrosion
Hybrid coating
Sol–gel

ABSTRACT

This work studies the synthesis and characterization of hybrid organic–inorganic coatings based on silica to improve the corrosion resistance of carbon steel. Hybrid organic–inorganic silica sol–gel coatings were obtained by dipping in an organically modified silica sol synthesized through hydrolysis and condensation of 3-glicidoxipropyl-trimetoxisilano (GPTMS) and tetraethoxysilane (TEOS) in acidic catalysis. The coatings were doped with a cerium salt ($Ce(NO_3)_3 \cdot 6H_2O$) and loaded with silica nanoparticles in order to improve both barrier effect and the anticorrosive behavior of the coatings by the inhibitory effect of cerium. Prior to the application of the coating, some samples were treated with a phosphoric acid 2% v/v in order to improve coating adherence. A two layered coating was applied onto AISI 1010 carbon steel, the outer containing with a cerium salt and the inner one with silica nanoparticles without the cerium salt, producing homogeneous and cracks-free films. Raman spectroscopy was used to characterize the compounds present in the surface of steel after pretreatment with phosphoric acid. Microstructural characterization of coatings was performed by means of scanning electron microscopy (SEM).
The evolution with time of the protective properties of films was studied by electrochemical impedance spectroscopy (EIS), providing quantitative information of the role of the pre-treatment. Electrochemical behavior in each stage of the corrosion processes was modeled by equivalent circuits. Additionally, films adhesion was evaluated by nano-scratch demonstrating that the phosphate treatment improves adhesion of the hybrid coating.

1. Introduction

One of the most common problems in industry related to materials is the damage that they suffer due to corrosion processes. Carbon steel is widely used in industry; however its susceptibility to corrosion in many environments limits its applications. For many years, chromate conversion coatings have been widely applied for corrosion protection of metals. However, the carcinogenic effect of chromate has generated serious environmental and health problems, for that reason its use is prohibited [1]. The application of hybrid organic–inorganic sol–gel coatings on different substrates has been thoroughly investigated in the last years [2–4]. Sol gel process is a chemical method that allows the synthesis of glassy and ceramic materials at lower temperatures than the conventional methods and can be used to obtain functionalized coatings. The corrosion behavior of sol–gel coatings has been extensively studied on various substrates, such as aluminum alloys [5–7], mild steel [8–11], stainless steel [12–14], galvanized steel [15,16] and others metals [2]. One strategy to minimize the corrosive attack is the application of coatings containing rare earth (RE) salts due to their low toxicity and environmental feasibility [17,18]. Dip-coating process is one of the most used methods for deposition of sol–gel coatings; this consists in the immersion of the substrate in the sol with a subsequent withdrawal at a controlled rate. The fast solvent evaporation produced during drying leads to solidification of the thin film deposited on the substrate. The presence of organic components within the inorganic silica network increases the ductility and the critical thickness of coatings allowing an increment on their protective character [19].

Tetraethoxysilane (TEOS) is one of the most common precursors for sol–gel coatings, its hydrolytic condensation provides of a 3D silica network which needs a thermal treatment upon 500 °C to reach an optimal densification. In order to achieve a crosslinked structure at lower temperatures and increase film plasticity, organic polymerization of a superimposed network should be performed. Glycidoxypropyl-trimethoxysilane (GPTMS) is an epoxy-functionalized alkoxyde able to promote both the hydrolytic condensation of a silica network and an organic polymerization of its epoxy rings producing a highly crosslinked hybrid network [20].

Addition of inhibitors into the sols has been widely studied being cerium salts one of the most documented [21–28]. Ce^{3+} and Ce^{4+}

* Corresponding author. Tel.: +54 2234816600; fax: +54 2234810046.
E-mail address: smcere@fi.mdp.edu.ar (S. Ceré).

0257-8972/$ – see front matter © 2012 Elsevier B.V. All rights reserved.
http://dx.doi.org/10.1016/j.surfcoat.2012.07.086

contained in the coating have a high reactivity with oxygen, being the driving force for their migration through the coating and reaction with the groups OH^- present at defective areas or where the film was damaged. Cerium hydroxides/oxides precipitate on cathodic sites and provide a local and natural barrier to later corrosion processes constituting a phenomenon of self-healing [7,22,29] Additionally, in an effort to improve the corrosion resistance, the incorporation of SiO_2 nanoparticles to the films had been used in order to increase coating thickness and density [30–33].

One of the main problems when applying sol–gel coatings on iron based alloys is the lack of adherence of the film formed on a substrate that easily oxidizes forming bulky oxides as Fe_2O_3. The use of phosphate conversion treatments has been studied in the past years in order to improve coatings adhesion [34,35].

This work evaluates the effect of a pretreatment with phosphoric acid on the corrosion behavior of carbon steel coated by the sol–gel method. TEOS and GPTMS were used as precursors; hybrid sols were loaded with SiO_2 nanoparticles and doped with cerium salts. The effect of the phosphate treatment on the coating performance was studied using classical electrochemical techniques as polarization curves and EIS; additionally, coating adherence was evaluates by nano-scratch.

2. Experimental

2.1. Materials and samples preparation

Nanostructured hybrid films were synthesized by the sol–gel route from TEOS (Fulka, Germany) and GPTMS (Dow Corning, USA) using a colloidal silica suspension (Ludox AS-40, Sigma Aldrich, USA) to improve mechanical and barrier properties, and $Ce(NO_3)_3 \cdot 6H_2O$ (Sigma Aldrich) as a supplier of Ce(III). Sols were prepared keeping molar ratios of TEOS/GPTMS/SiO2 = 42/18/40 (for so-called TGS sol) and TEOS/GPTMS/Ce = 66.5/28.5/5 (for the TGC sol), both in acidic conditions. Cerium nitrate hexahydrate was dissolved in ethanol and then mixed with TEOS and GPTMS keeping the relationship of 5% in moles in the sol stated above for the sol containing Ce (TGC). 0.1 mol dm^{-3} HNO3 solution was used both as a water source and catalyzer in the TGC sol. The system was magnetically stirred for 2 h at room temperature. The TGS sol was prepared by high speed stirring of TEOS, GPTMS and silica nanoparticles, to promote the homogenization of the immiscible phases producing a thin emulsion prior the addition of concentrated nitric acid to catalyze the reactions. A transparent and colorless sol was obtained. The sol was also stirred for 2 h at room temperature.

Carbon steel plates, AISI 1010, (Timar SRL, Argentina) previously polished with emery paper up to grade 400, degreased with ethanol and rinsed with distilled water, were used as substrates. Table 1 shows the chemical composition of substrates analyzed by spark emission spectroscopy (BAIRD DV6 with MC20 processor, Baird Corporation, 1996, USA).

In order to study the influence of phosphoric acid pretreatment on the corrosion resistance and film adherence on the coated samples, half of the samples were immersed in a solution of phosphoric acid 2% v/v for 10 min at room temperature (20 ± 1 °C). With the aim of clarity, samples with phosphoric treatment are named as "P" meanwhile the ones without phosphoric treatment are referred as "B" along this work. Sol–gel coatings were applied by dipping using a withdrawal speed of 3 cm min^{-1} for the first layer (TGS) and 35 cm min^{-1} for the second layer (TGC). Glass slides were also coated with single layers of both sols for thickness measurement.

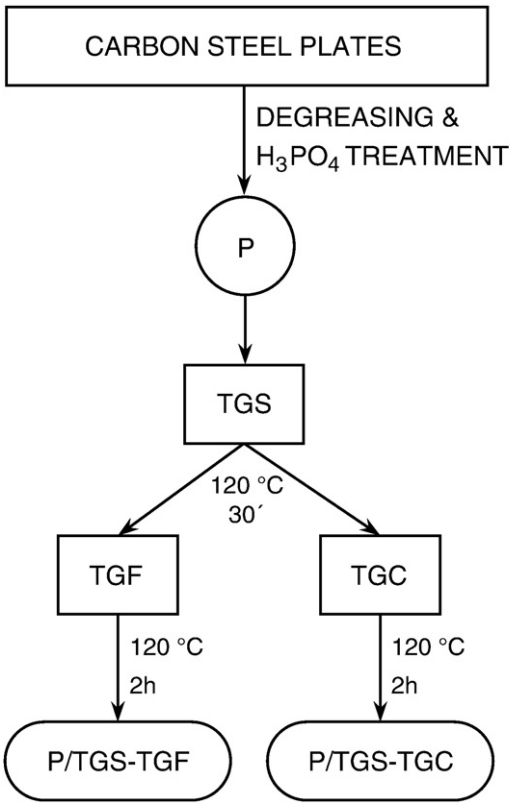

Fig. 1. Sketch of deposition procedure for steel plates.

Deposition procedure for steel plates is sketched in Fig. 1.

2.2. Surface characterization and electrochemical measurement

Microstructural characterization of substrates and sol–gel coatings was performed by optical microscopy (Olympus PMG3, Japan) and scanning electron microscopy (SEM/EDS, Jeol 6460, Japan).

Roughness was measured on substrates and coated samples using a profilometer (Surtronic 3^+, Taylor-Hobson, UK) with a vertical resolution of 0.02 μm. Data were processed with Taly Profile Gold software. A cut-off of 0.8 mm and a measurement length of 4 mm were used. Four independent measurements were performed on each sample.

The crystalline phases present in the surface compounds on the steel, with and without pretreatment, were determined by Raman spectroscopy using an Invia Reflex confocal Raman microscope (Renishaw, UK) in order to determine surface composition and to establish if any compounds coming from the bath are incorporated to the final structure of the film. The Raman spectra were obtained using an argon laser of 514 nm (25 mW) in backscattering mode with a laser spot of 10 μm. An exposure time of 20 s and 3 accumulations were used, with 50× objective. No thermal effects were observed on the samples during these measurements.

Table 1
Chemical composition (wt.%) of mild steel obtained by spark emission spectroscopy.

Element	Fe	C	S	P	Mn	Si	Mo
wt.%	Balance	0.003 ± 0.0002	0.009 ± 0.002	0.015 ± 0.0003	0.153 ± 0.006	0.0014 ± 0.0003	0.006 ± 0.002

Coating thickness was measured on glass samples after densification by means of a profilometer (Talystep, Taylor-Hobson, UK) on a scratch made immediately after deposition. The coating thickness was stated as the average of at least five independent measurements on each sample.

2.3. Electrochemical characterization

The corrosion resistance was evaluated by means of potentiodynamic polarization tests and electrochemical impedance spectroscopy (EIS) measurements using a 0.35% w/v NaCl solution prepared from p.a. grade chemicals (Sigma-Aldrich) and bidistilled water (Millipore, 18.2 MΩ cm). Both electrochemical measurements were carried out by using a typical three-electrode configuration using a saturated calomel electrode (SCE, Radiometer Analytical, France) as the reference electrode, a platinum wire of convenient area as counter electrode and the material to be tested as working electrode (WE). All the potentials in this work are referred to SCE. The working electrode was placed in the bottom of the cell, delimiting an area of 3.54 cm^2. EIS was performed sweeping frequencies from 50,000 to 0.01 Hz and modulating ±0.01 V (rms) around the corrosion potential (E_{corr}). Potentiodynamic polarization curves were scanned from the corrosion potential to 1 V at a rate of 0.002 V s^{-1} and backwards. All of the tests were performed at room temperature (20 ± 1 °C). EIS fitting was performed using Zplot software [36].

2.4. Adhesive characterization

One of the most recent techniques used to study the adhesion of thin films consists in the measurement of quasi-statically penetration of an indenter at increasing loads applied to a material. The nano-scratching test is implemented with a modulus of lateral force and a ramped load in the displacement path (scratch) [37,38].

The nano-scratch tests were performed using a nano-indenter XP, MTS Nano Instruments (MTS Nano Instruments, US) (force resolution: 50 nN; displacement resolution: 0.1 nm) equipped with a nano-scratch attachment that allows lateral force measurements. A pyramidal diamond Berkovich indenter was used to scratch each coating/substrate system and a 700 μm scratching track was applied in all tests. In a first step (pre-scan), an initial surface profile of the samples is made before scratching by a depth-sensing system. The tip approaches the surface under standard conditions; the load is maintained (0.1 mN) through all the scratch distance (100 μm initial + 500 μm straightforward scratch + 100 μm final). In the second step (scratching), the tip starts scratching at 100 μm from the start point with a ramped load (final maximum applied load of 200 mN) to the distance of 600 μm, corresponding to an effective scratch distance of 500 μm, where the load is removed to the initial one (0.1 mN) and maintained constant for 100 μm more. In all cases the scratch testing was done with an edge of the Berkovich tip pointing in the direction of the scratch. As last step (post-scan), using the same conditions of the first one, a final surface profile was determined to measure the elastic recovery after scratching. The results are presented as the average of five independent determination on each sample.

Lateral (friction) forces were calculated from the deflection of the loading column. The coefficient of friction (COF) was calculated by taking the ratio of the lateral force and the normal load applied on the indenter afterwards [39].

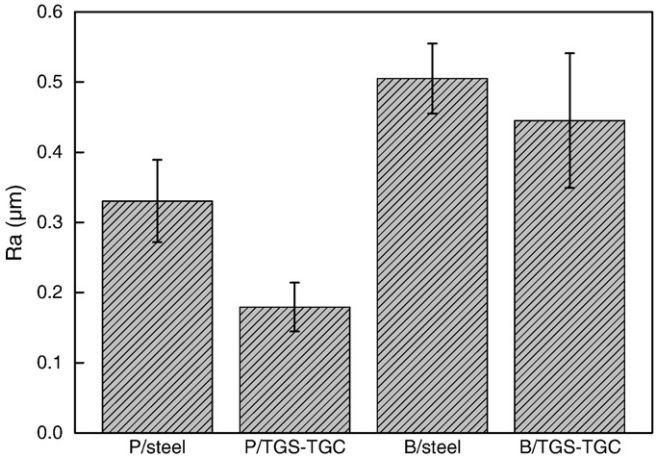

Fig. 3. Roughness measurements of P/steel, P/TGS–TGC, B/steel and B/TGS–TGC.

3. Results and discussion

3.1. Characterization of sols and coatings

Fig. 2 shows SEM micrographs of B/ and P/steel. It can be observed that there are some differences in the morphology that can be clearly distinguished, regarding the surface modification produced by the acid treatment. Additionally, sample surface roughness decreased with the pretreatment as shown in Fig. 3. This reduction has already been observed for other systems where acidic treatment produces a smothering of the macro topography [40].

Fig. 4 compares the Raman spectra of B/ and P/steel. All the peaks for P/steel can be reasonably assigned to hematite (Fe_2O_3) and

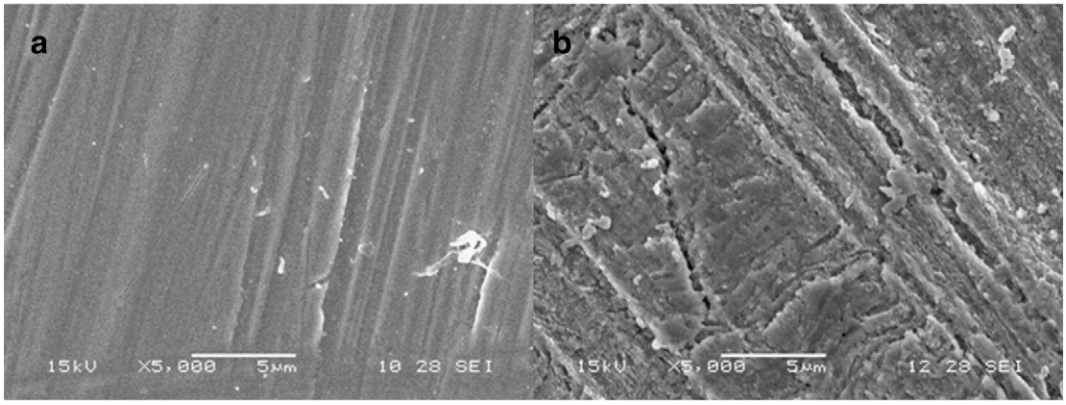

Fig. 2. SEM micrographs of B/steel (a) and P/steel (b).

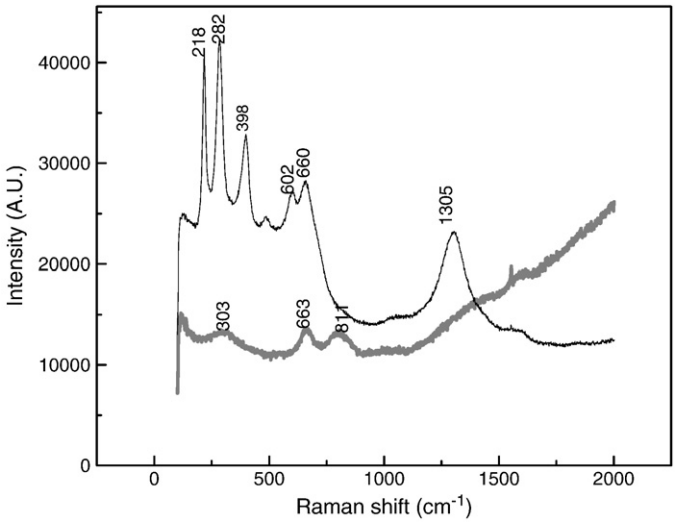

Fig. 4. Raman spectra obtained for B/steel (—) and P/steel (—).

magnetite (Fe_3O_4) despite a shift of approximately 8 cm^{-1} observed compared with hematite powder [41]. For the B/steel the main peaks correspond to hematite although the spectrum is not well defined. Table 2 shows a comparison of the results with those corresponding to hematite and magnetite.

Transparent, homogeneous and crack-free sol–gel coatings were obtained after thermal treatment. Coatings obtained using TGS sol were transparent and the ones using TGC sol were slightly yellowish. Table 3 shows the measured thickness for the single coatings applied on glass. It can be observed that the presence of silica nanoparticles increases coating thickness.

Fig. 5 shows micrographs of B/TGS–TGC and P/TGS–TGC. The original morphology was completely covered by the sol–gel coatings. It can also be observed in Fig. 3 that roughness diminish after coating following the same trend than the bare substrate.

3.2. Electrochemical behavior

Fig. 6 shows the anodic polarization curves for the systems P/TGS–TGC and B/TGS–TGC and their comparison with the two surface treatments without coating (B/ and P/steel) after 24 h of immersion in 0.35% w/v NaCl. All the curves, but the corresponding to P/TGS–TGC, present active dissolution showing a monotonic increase of current density with potential. The system B/TGS–TGC, although shows active dissolution, presents a reduction in current density when compared with the uncoated ones. The reduction in current density can be attributed to a reduction of the active area. Also, a shift of the corrosion potential to more positive values together with a region of constant low current density is observed for the system P/TGS–TGC bringing a significant improvement in corrosion resistance the coated carbon steel.

EIS diagrams in the Bode format are presented in Figs. 7 and 8 for the coated samples applied on B/ and P/steel immediately after immersion (t_0) and after 24 h of immersion in 0.35% w/v NaCl

Table 2
Comparison of Raman spectral peaks observed for P/steel and B/steel with literature data for magnetite and hematite [41].

Hematite	225_{sh}	245	290_{sh}	412	500	611	661	817	1321_{sh}
Magnetite			310		540		670_{sh}		
P/steel	218		282	398		602	660		1305
B/steel			303				663	811	

Table 3
Coatings thickness measured by profilometry. Vertical resolution 0.02 μm.

Coating	Thickness (μm)
TGS	3.29 ± 0.08
TGC	2.45 ± 0.16

respectively. It can be observed in Fig. 7, for very short immersion times, that both coated samples present a typical response of a protective coating disregard the pre-treatment done. However, after 24 h immersion in the electrolyte (Fig. 8) the B/TGS–TGC coating shows a notorious decrease in the phase angle in the high frequency region together with a drop in the impedance modulus, denoting a great deterioration of the film reaching values comparable to the ones of B/steel after the same period of immersion. This result takes into account the massive defects developed in the coating after immersion. Although the P/TGS–TGC coating shows some extent of deterioration with the appearance of a resistive domain at intermediate frequencies, the impedance modulus remains higher than the P/steel showing a protective feature on the substrate.

To get a better insight in the coating and substrate behavior, the EIS data were fitted by means of equivalent circuits using Zplot for Windows [36], relating the high frequency component of the Bode plot to the electrical properties of the film present on the surface. The solid lines in Figs. 7 and 8 show the data fitting for each condition studied using the circuits shown in Fig. 9. For the analysis of the EIS results, a constant phase element impedance contribution (Z_{CPE}) was used [42] taking in account the deviations from a slope of −1 in the modulus Bode plot. Z_{CPE} is given by:

$$Z_{CPE} = 1/Q(j\omega)^{\alpha} \tag{1}$$

where Q is a parameter independent of frequency and α is a coefficient associated with system homogeneity [43,44]. The origin of a CPE response is related to a distribution of time constants, but a great variety of explanations are reported in literature. [45,46].

Considering a resistive-capacitive parallel circuit ($Z_{R//CPE}$) and using a CPE instead an ideal capacitor, the impedance for the circuit arrangement is given by Eq. (2):

$$Z_{R//CPE} = \frac{R}{1 + QR(j\omega)^{\alpha}}. \tag{2}$$

Where R is the resistance in parallel with the CPE and Q and α have the same meaning than in Eq. (1). For a symmetric distribution of relaxation times, the Cole–Cole [47,48] model gives a depressed semicircle in the Nyquist plot, and its impedance response is given in Eq. (3).

$$Z_{R//CPE} = \frac{R}{1 + \left(j\omega RC_{eff}\right)^{\alpha}} \tag{3}$$

Where C_{eff} is the effective capacitance associated with the impedance response. Equating Eqs. (2) and(3), the expression for the effective capacitance as a function of R and Z_{CPE} can be obtained (Eq. (5)).

$$QR(j\omega)^{\alpha} = (j\omega RC)^{\alpha} \tag{4}$$

$$C_{eff} = \frac{(QR)^{1/\alpha}}{R} \tag{5}$$

Three different electrical circuits were used to fit the experimental data (Fig. 9). These has been discussed and used extensively in the literature [49–52]. For all of them, R_e is associated with the solution

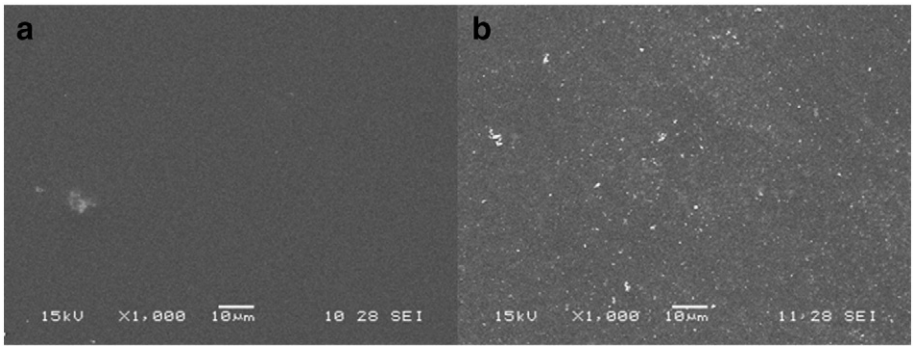

Fig. 5. SEM micrograph of B/TGS–TGC (a) and P/TGS–TGC (b).

resistance. Circuits shown in Fig. 9a are used for porous oxides and porous defective coating applied on metals. R_{po} is the "pore resistance" coming from the penetration of the electrolyte creating an ionically conducting path through the coating and Q_{coat} is the pseudocapacitance associated to the coating while Q_{dl} and R_{ct} are the variables associated to the double layer pseudocapacitance and charge transfer resistance respectively. Constant phase element contributions are included here since the system presents frequency dispersion associated with relaxation phenomena, probably due to solvent incorporation in the film. Circuit a1 was used to fit P/steel in both immersion periods and B/steel immediately after immersion and a2 was used for P/TGS–TGC after 24 h of immersion. Circuit shown in Fig. 9b shows only and resistive capacitive mesh associated to impedance response where only a time constant is evident. This circuit was used for B/steel and B/TGSTGC after 24 h of immersion. For the coated samples immediately after immersion, improvements to the fittings were obtained by adding a third resistive-capacitive component as shown in circuit c. In this case the third component in the intermediate frequency is related to the oxide where the resistance corresponding to the film (R_{ox}) is in parallel with the interfacial impedance of a leaky dielectric (Q_{ox}) barrier layer associated with the capacitance of the oxide film in contact with the substrate and the time constant at low frequency is related to the corrosion process on the metal surface where R_{ct} and Q_{dl} can be correlated to charge transfer resistance and the double layer pseudocapacitance as indicated above. [53,28]. Fitting parameters are shown in Table 4. Regarding the uncoated system, B/ and P/steels immediately after immersion, show the same corrosion behavior, but after 24 h the impedance response in B/steel is dominated for the oxide formed onto the surface and it is not possible to separate the contributions of the oxide from the metal/electrolyte interface. Both coated systems present comparable response immediately after immersion in NaCl with very low capacity and high resistance. After immersion, the P/TGS–TGC shows still low capacitance and high resistance but the B/TGS–TGC shows a decrease in the resistance together with an increase in the capacitance denoting the electrolyte diffusion into the coating. It can be observed that although both systems shows signs of deterioration after immersion, P/TGS–TGC present higher R_{po} and lower $C_{effcoat}$ than B/TGS–TGC denoting that the phosphate pretreatment has a beneficial effect on coating performance in aggressive environments.

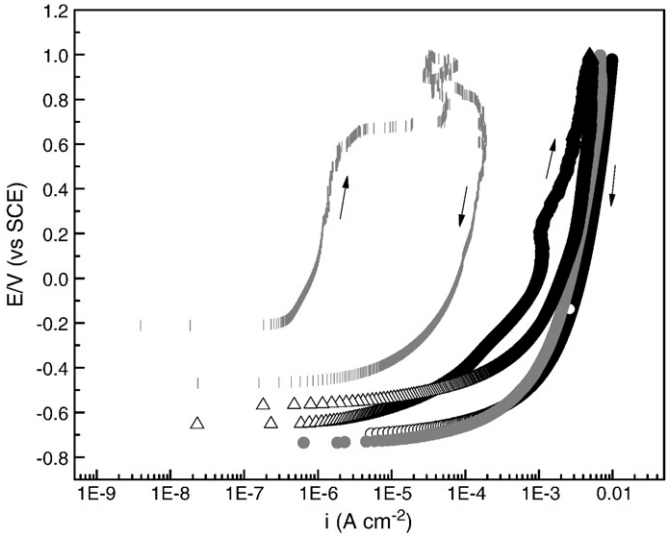

Fig. 6. Potentiodynamic polarization curves after 24 h of immersion for in 0.35% w/v NaCl solution. B/steel (○), P/steel (•), P/TGS–TGC (|) and B/TGS–TGC (Δ). Sweep rate = 2 mV s^{-1}.

3.3. Adhesive characterization

The adhesive and frictional behavior of the two types of films was analyzed with the results of the nano-scratch tests with the principal aim to find and analyze the critical load, *Lc*, when a well defined failure event occurs. If the failure event represents coating detachment then the critical load can be used as a quantitative measure of the coating–substrate adhesion.

Fig. 10a and b shows the surface profiles of the steel plates B/TGS–TGC and P/TGS–TGC, respectively.

The scratch depths (nm) are plotted as a function of both the horizontal displacements (μm) and the normal load applied (mN). The curves illustrate the sample behavior during the pre-scan, scratching and post-scan steps. The initial scan at a continuous low load applied is used to analyze the roughness of the film surface through the obtained profile. This profile is used, in relation to the post-scan, in order to evaluate surface damage, debris production and elastic–plastic deformation after the scratching.

As can be seen in Fig. 10a, the critical load to produce the failure of the coating for the untreated steel surface is 134 ± 29 mN, after an almost total elastic recovery at previous applied loads. This adhesion force and the post-scan curve show clear fracture processes at early times, indicating some delamination events that could lead to fracture and material release to the sides of the indentation trace. The influence of the phosphoric treatment can be clearly observed with the scratch profile of the P/TGS–TGC sample shown in Fig. 10b. In this case the failure takes place at 296 ± 53 mN of applied load, indicating a much better adhesion of the hybrid coating than the system without the phosphoric acid treatment. The peak present in the post-scan around the 400 μm scratch distance position can be attributed to the presence of debris in the trace, showing a slight failure in the coating. This fact, typical for vitreous and hybrid coatings, could be

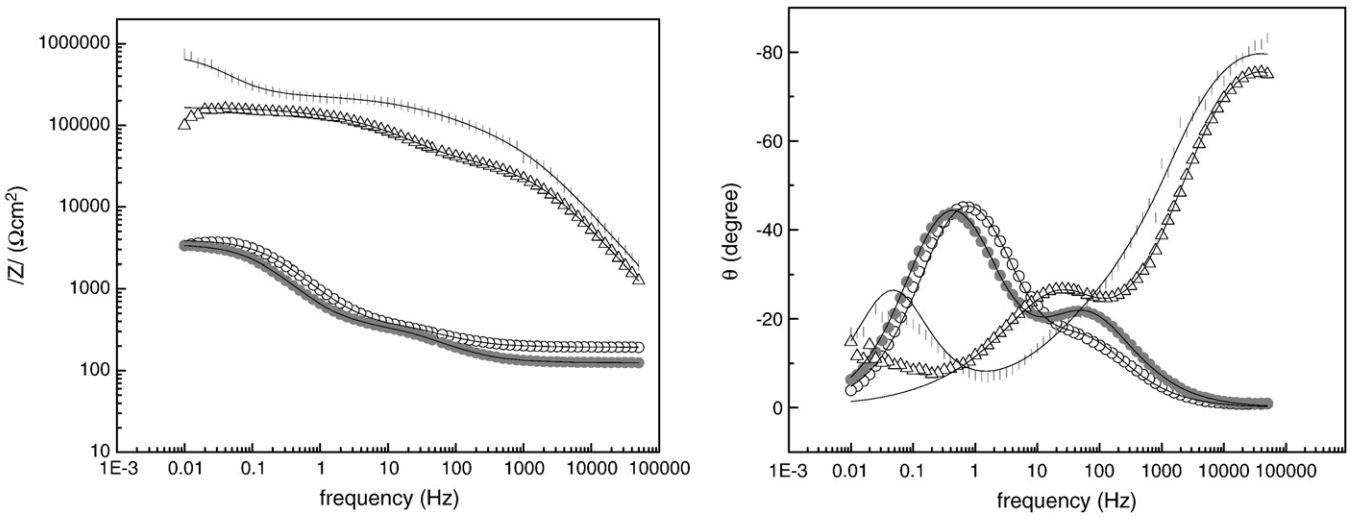

Fig. 7. EIS Bode plots obtained for for B/steel (○), P/steel (∘), P/TGS–TGC (|) and B/TGS–TGC (Δ) immediately after immersion in 0.35% w/v NaCl solution. Solid lines correspond to the fitting according the circuits shown in Fig. 9.

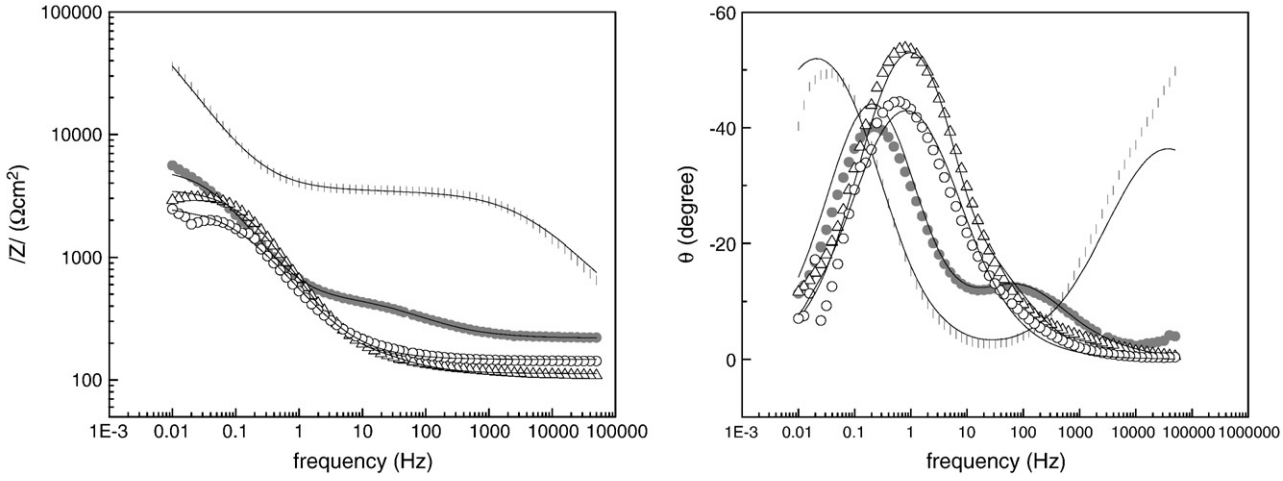

Fig. 8. EIS Bode plots obtained for for B/steel (○), P/steel (∘), P/TGS–TGC (|) and B/TGS–TGC (Δ) after 24 h of immersion in 0.35% w/v NaCl solution. Solid lines correspond to the fitting according the circuits shown in Fig. 9.

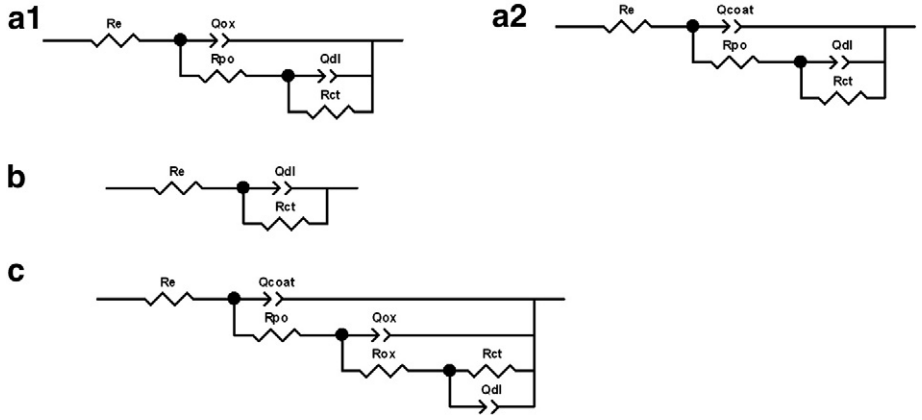

Fig. 9. Equivalent circuits employed for data fitting: P/steel immediately after immersion (t_0) and after 24 h immersion and B/steel immediately after immersion (a1) and P/TGS–TGC and B/TGS–TGC after 24 h of immersion in NaCl solution (a2), B/steel after 24 h immersion (b), P/TGS–TGC and B/TGS–TGC immediately after immersion in 0.35% w/v NaCl (c).

due to the presence of chipping produced by radial cracks formation and its subsequent delamination [54,55]. Fig. 11 shows the scratch image of the sol gel coatings on carbon steel. In Fig. 11a, the early breakdown and chipping of the B/TGS–TGC system can be clearly identified as well as the radial cracks around both analyzed samples. This is not observed in the system P/TGS–TGC (Fig. 11b).

Table 4
EIS data fitting using the different equivalent circuits shown in Fig. 9. B/ and P/steel (a) B/TGS–TGC and P/TCS–TGC (b).

	R_e (Ω cm^2)	Q_{ox} ($s^{\alpha}\ \Omega^{-1}$ m^{-2})	α_{ox}	R_{dox} (Ω cm^2)	C_{effox} (F cm^{-2})	Q_{dl} ($s^{\alpha}\ \Omega^{-1}$ cm^{-2})	α_{dl}	R_{pol} (Ω cm^2)	$C_{eff\ d}$ (F cm^{-2})
B to	213.3 ± 1.98	$6.9\times10^{-5}\pm7.6\times10^{-6}$	0.81 ± 0.02	208.2 ± 13.2	2.56×10^{-5}	$2.1\times10^{-4}\pm1.2\times10^{-6}$	0.93 ± 0.013	$1.8\times10^{3}\pm33.2$	1.9×10^{-4}
B 24 h	146.8 ± 0.97	–	–	–	–	$5.2\times10^{-4}\pm8.9\times10^{-6}$	$0.72 \pm 6.3\times10^{-3}$	$2.4\times10^{3}\pm49.7$	5.7×10^{-4}
P to	124.5 ± 0.26	$8.1\times10^{-5}\pm3.2\times10^{-6}$	$0.74 \pm 5.9\times10^{-3}$	285.1 ± 4.4	2.13×10^{-5}	$3.8\times10^{-4}\pm3.5\times10^{-6}$	$0.85 \pm 3.5\times10^{-3}$	$3.1\times10^{3}\pm12.2$	3.9×10^{-4}
P 24 h	218.5 ± 3.09	$1.1\times10^{-4}\pm3.3\times10^{-5}$	0.63 ± 0.05	283 ± 30.4	1.32×10^{-5}	$4.9\times10^{-4}\pm3.5\times10^{-5}$	0.83 ± 0.02	$4.9\times10^{3}\pm135.8$	5.9×10^{-4}

	R_e (Ω cm^2)	Q_{coat} ($s^{\alpha}\ \Omega^{-1}$ cm^{-2})	α_{coat}	R_{po} (Ω cm^2)	$C_{effcoat}$ (F cm^{-2})	Q_{ox} ($s^{\alpha}\Omega^{-1}$ cm^{-2})	α_{ox}	R_{dox} (Ω cm^2)	C_{effox} (F cm^{-2})	Q_{dl} ($s^{\alpha}\ \Omega^{-1}$ cm^{-2})	α_{dl}	R_{ct} (Ω cm^2)	$C_{eff\ dl}$ (F cm^{-2})
B/TGS–TGC to	109 ± 1.1	$6.1\times10^{-9}\pm2.3\times10^{-10}$	$0.93\pm2.9\times10^{-3}$	$1.8\times10^{4}\pm1.1\times10^{3}$	3.07×10^{-9}	$9.6\times10^{-7}\pm5.0\times10^{-8}$	0.47 ± 0.011	$4.4\times10^{4}\pm2.8\times10^{3}$	2.97×10^{-8}	$1.8\times10^{-7}\pm3\times10^{-8}$	0.84 ± 0.03	$1.0\times10^{5}\pm3.5\times10^{3}$	8.50×10^{-8}
B/TGS–TGC 24 h	117.3 ± 1.06	$3.6\times10^{-4}\pm7.1\times10^{-6}$	0.76 ± 0.007	$3.6\times10^{3}\pm76.9$	4.02×10^{-4}	–	–	–	–	–	–	–	–
P/TGS–TGC to	109 ± 1.1	$3.4\times10^{-9}\pm4.4\times10^{-10}$	0.94 ± 0.01	$4.5\times10^{4}\pm8.1\times10^{3}$	2.02×10^{-9}	$2.9\times10^{-7}\pm3.8\times10^{-8}$	0.5 ± 0.03	$1.9\times10^{5}\pm1.3\times10^{4}$	1.81×10^{-8}	$1.1\times10^{-5}\pm6.2\times10^{-7}$	0.95 ± 0.05	$2.8\times10^{5}\pm2.9\times10^{4}$	1.18×10^{-5}
P/TGS–TGC 24 h	109 ± 1.1	$3.2\times10^{-7}\pm9.2\times10^{-9}$	$0.67\pm2.5\times10^{-3}$	$3.4\times10^{3}\pm9.12$	1.11×10^{-8}	–	–	–	–	$2.03\times10^{-4}\pm9.4\times10^{-7}$	$0.80\pm3\times10^{-3}$	$7.0\times10^{4}\pm1.5\times10^{3}$	3.94×10^{-4}

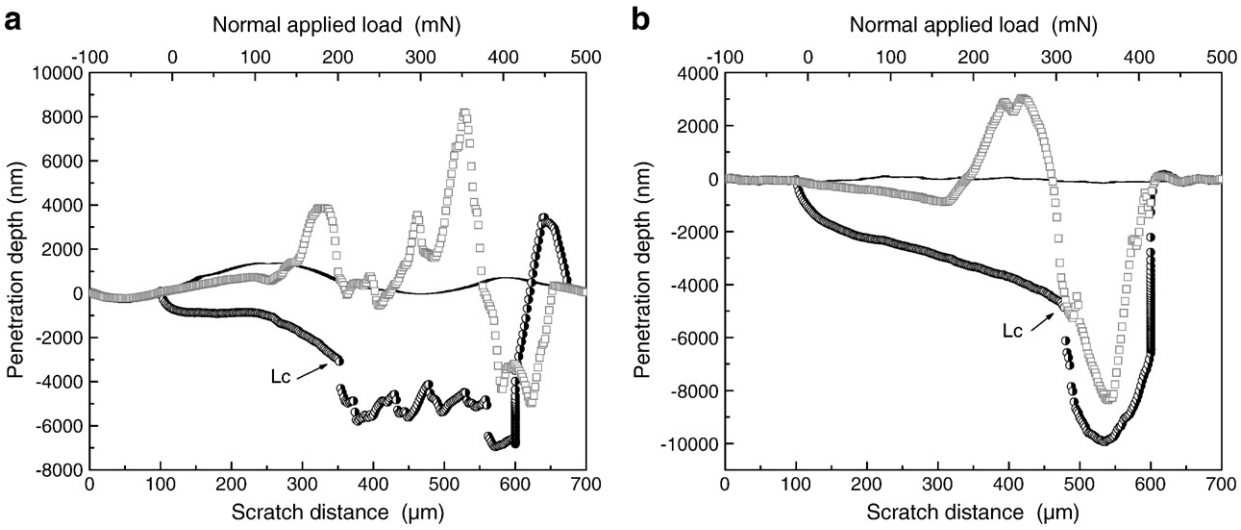

Fig. 10. Scratch depth profile as a function of increasing normal load and as a function of displacement of the indenter tip for B/TGS–TGC (a) and P/TGS–TGC steel (b) samples. The pre-scan (–), scan (●) and post-scan (◦) made are shown.

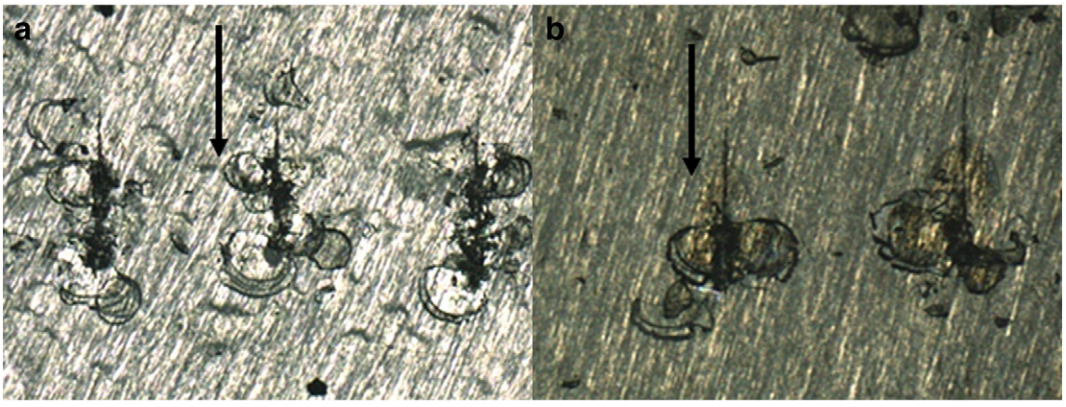

Fig. 11. Scratch image of the sol–gel coatings on carbon steel: B/TGS–TGC (a) and P/TGS–TGC (b). The arrow indicates the scratch direction.

4. Conclusions

Coatings produced by dipping by sol gel technique were studied for corrosion protection of carbon steel. In order to enhance coating protection, since the lack of adherence due to the formation of bulky iron oxides in a concern, a pretreatment with phosphoric acid was applied prior to coating deposition.

A bilayered sol–gel coating was deposited on carbon steel substrates in order to improve its corrosion behavior. The dip-coating process of the former layer, with barrier properties, and the second one, functionalized with cerium salts, addressed to a homogeneous, adherent and protective coating system.

In order to get a stronger adhesion of coatings and a further enhancement of the anticorrosive behavior, a pretreatment of steel substrates with phosphoric acid was evaluated.

Phosphoric pretreatment promoted the formation of hematite and magnetite crystals on the steel surface. This feature was accompanied by an increase of approximately a 120% of the critical load of failure and an improvement of the corrosion resistance of the films when the phosphoric acid pretreatment is done.

Acknowledgments

The support from the Consejo Nacional de Investigaciones Científicas y Técnicas, Agencia Nacional de Promoción Científica y Tecnológica (PICT 1144/07) and the Universidad Nacional de Mar del Plata, Argentina is gratefully acknowledged. The authors also acknowledge Drs. Procaccini, Valcarce, Ballarre and Eng. Echeverria (INTEMA, Argentina) by their support on thickness, Raman, adherence and roughness measurements.

References

[1] J.H. Osborne, Prog. Org. Coat. 41 (2001) 280.
[2] D. Wang, G.P. Bierwagen, Prog. Org. Coat. 64 (2009) 327.
[3] A.N. Khramov, V.N. Balbyshev, L.S. Kasten, R.A. Mantz, Thin Solid Films 514 (2006) 174.
[4] M. Fallet, H. Mahdjoub, B. Gautier, J.-P. Baue, J. Non-Cryst. Solids 293–295 (2001) 527.
[5] V. Palanivel, Y. Huang, W.J. Van Ooij, Prog. Org. Coat. 53 (2005) 153.
[6] A. Pepe, M. Aparicio, S. Cere, A. Duran, J. Non-Cryst. Solids 348 (2004) 162.
[7] Hongwei Shi, Fuchun Liu, Enhou Han, Mat. Chem. Phys. 124 (2010) 291.
[8] A. Pepe, P. Galliano, M. Aparicio, A. Duran, S. Cere, Surf. Coat. Technol. 200 (2006) 3486.
[9] Alka Phanasgaonkar, V.S. Raja, Surf. Coat. Technol. 203 (2009) 2260.
[10] P.H. Suegama, H.G. de Melo, A.A.C. Recco, A.P. Tschiptschin, I.V. Aoki, Surf. Coat. 202 (2008) 2850.
[11] Min Qian, A.M. Soutar, Xiu H. Tan, Xian T. Zeng, S.L. Wijesinghe, Thin Solid Films 517 (2009) 5237.
[12] S.M. Hosseinalipour, A. Ershad-langroudi, Prog. Org. Coat. 67 (2010) 371.
[13] J. Ballarre, E. Jimenez-Pique, M. Anglada, S.A. Pellice, A.L. Cavalieri, Surf. Coat. Technol. 203 (2009) 3325.
[14] Y. Castro, A. Duran, J.J. Damborenea, A. Conde, Electrochim. Acta 53 (2008) 6008.
[15] S. Dalbin, G. Maurin, R.P. Nogueira, J. Persello, N. Pommier, Surf. Coat. Technol. 194 (2005) 363.
[16] M.G.S. Ferreira, R.G. Duarte, M.F. Montemor, A.M:.P. Simões, Electrochim. Acta 49 (2004) 2927.
[17] Tianlan Peng, Ruilin Man, J. Rare Earths 27 (2009) 159.
[18] A. Kartsonakis, I. Daniilidis, G.C. Kordas, J. Sol–Gel Sci. Technol. 48 (2008) 24.
[19] V. Palanivel, D. Zhu, W.J. Van Ooij, Prog. Org. Coat. 47 (2003) 384.
[20] S.R. Davis, A.R. Brough, A. Atkinson, J. Non-Cryst. Solids 315 (2003) 197.

[21] M. Garcia-Heras, A. Jimenez-Morales, B. Casal, J.C. Galvan, S. Radzki, M.A. Villegas, J. Alloys Compd. 380 (2004) 219.
[22] N. Pirhady Tavandashti, S. Sanjabi, Prog. Org. Coat. 69 (2010) 384.
[23] M.L. Zheludkevich, R. Serra, M.F. Montemor, K.A. Yasakau, I.M. Miranda Salvado, M.G.S. Ferreira, Electrochim. Acta 51 (2005) 208.
[24] M. Zaharescu, L. Predoana, A. Barau, D. Raps, F. Gammel, N.C. Rosero-Navarro, Y. Castro, A. Duran, M. Aparicio, Corros. Sci. 51 (2009) 1998.
[25] I.A. Kartsonakis, A.C. Balaskas, G.C. Kordas, Corros. Sci. 53 (2011) 3771.
[26] H. Wang, R. Akid, Corros. Sci. 50 (2008) 1142.
[27] L. Paussa, N.C. Rosero Navarro, D. Bravin, F. Andreatta, A. Lanzutti, M. Aparicio, A. Duran, L. Fedrizzi, Prog. Org. Coat. 74 (2012) 311.
[28] N.C. Rosero-Navarro, L. Paussa, F. Andreatta, Y. Castro, A. Durán, M. Aparicio, L. Fedrizzi, Prog. Org. Coat. 69 (2) (2010) 167.
[29] W. Trabelsi, P. Cecilio, M.G.S. Ferreira, M.F. Montemor, Prog. Org. Coat. 54 (2005) 276.
[30] W.J. van Ooij, D. Zhum, M. Stacy, A. Tumgada, J. Gandhi, P. Puomi, Tsinghua Sci. Technol. 10 (2005) 639.
[31] P.H. Suegama, A.A.C. Recco, A.P. Tschiptschin, I.V. Aoki, Prog. Org. Coat. 60 (2007) 90.
[32] P.H. Suegama, H.G. Melo, A.A.C. Recco, A.P. Tschiptschin, I.V. Aoki, Surf. Coat. Technol. 202 (2008) 2850.
[33] S. Pellice, P. Galliano, Y. Castro, A. Durán, J. Sol–Gel Sci. Technol. 28 (2003) 81.
[34] C.N. Panagopoulos, E.P. Georgiou, M.G. Tsoutsouva, M. Krompa, J. Coat. Technol. Res. 8 (1) (2011) 125.
[35] G. Rubi, O.P. Modi, I.B. Singh, A.K. Jha, A.H. Yegneswaran, Surf. Coat. Technol. 201 (2006) 1866.
[36] Z Plot for Windows, Electrochemical Impedance Software Operating Manual: Part I, Scribner Associates, Inc., Southern Pines, NC, 1998.
[37] S. Simunkova, O. Blahova, I. Stepanek, J. Mater. Proc. Technol. 133 (1–2) (2003) 189.
[38] G. Wei, B. Bhushan, S. Joshua Jacobs, Ultramicroscopy 100 (3–4) (2004) 375.
[39] T.W. Scharf, J.A. Barnard, Thin Solid Films 308–309 (1997) 340.
[40] K.P. Rajurkar, J. Kozak, A. Chatterjee, ASM handbook surface engineering, ASM International, Materials Park, 5, OH, USA, 1996.
[41] M. Hanesch, Geophys. J. Int. 177 (2009) 941.
[42] J. Ross Macdonald, W.B. Johnson, Impedance Spectroscopy, Chapter one. John Wiley & Sons, New York, 1987.
[43] J.B. Jorcin, M.E. Orazem, N.P. Pébère, B. Tribollet, Electrochim. Acta 51 (2006) 1473.
[44] M. Orazem, B. Tribollet, Electrochem.Impedance Spectrosc.(ECS), John Wiley & Sons, New York, 2008.
[45] Chang-Hee Kim, Su-Il Pyun, Jong-Huy Kim, Electrochim. Acta 48 (2003) 3455.
[46] C.A. Schiller, W. Strunz, Electrochim. Acta 46 (2001) 3619.
[47] K.S. Cole, R.H. Cole, J. Chem. Phys. 9 (1941) 341.
[48] I.D. Raistrick, J. Ross Macdonald, D.R. Franceschetti, in: J. Ross Macdonald (Ed.), Emphasizing Solid Materials and SystemsJohn Wiley & Sons, New York, 1987.
[49] W. Tabelsi, Surf. Coat. Technol. 200 (2006) 4240.
[50] V.S. Sastri, Corrosion Inhibitors: Principles and Applications, John Wiley & Sons, New York, 1998.
[51] M.E. Orazem, B Tribollet, Chapter three Electrochemical Impedance Spectroscopy, Wiley, New Jersey, 2008.
[52] F. Mansfeld, J. Appl. Electrochem. 25 (1995) 187.
[53] P.L. Bonora, F. Deflorian, L. Fedrizzi, Electrochim. Acta 41 (78) (1996) 1073.
[54] J. Malzbender, J. den Toonder, A. Balkenende, G. de With, Mater. Sci. Eng., R. 36 (2002) 47.
[55] X. Zhang, L. Hu, D. Sun, Acta Mater. 54 (2006) 5469.